Sensitivity of a Cloud-Resolving Model to Bulk and Explicit Bin Microphysical Schemes. Part II: Cloud Microphysics and Storm Dynamics Interactions

XIAOWEN LI

Goddard Earth Science and Technology Center, University of Maryland, Baltimore County, Baltimore, Maryland

WEI-KUO TAO

Laboratory for Atmospheres, NASA Goddard Space Flight Center, Greenbelt, Maryland

ALEXANDER P. KHAIN

The Hebrew University of Jerusalem, Jerusalem, Israel

JOANNE SIMPSON

Laboratory for Atmospheres, NASA Goddard Space Flight Center, Greenbelt, Maryland

DANIEL E. JOHNSON

Goddard Earth Science and Technology Center, University of Maryland, Baltimore County, Baltimore, Maryland

(Manuscript received 12 October 2007, in final form 17 April 2008)

ABSTRACT

Part I of this paper compares two simulations, one using a bulk and the other a detailed bin microphysical scheme, of a long-lasting, continental mesoscale convective system with leading convection and trailing stratiform region. Diagnostic studies and sensitivity tests are carried out in Part II to explain the simulated contrasts in the spatial and temporal variations by the two microphysical schemes and to understand the interactions between cloud microphysics and storm dynamics. It is found that the fixed raindrop size distribution in the bulk scheme artificially enhances rain evaporation rate and produces a stronger near-surface cool pool compared with the bin simulation. In the bulk simulation, cool pool circulation dominates the near-surface environmental wind shear in contrast to the near-balance between cool pool and wind shear in the bin simulation. This is the main reason for the contrasting quasi-steady states simulated in Part I. Sensitivity tests also show that large amounts of fast-falling hail produced in the original bulk scheme not only result in a narrow trailing stratiform region but also act to further exacerbate the strong cool pool simulated in the bulk parameterization.

An empirical formula for a correction factor, $r(q_r) = 0.11q_r^{-1.27} + 0.98$, is developed to correct the overestimation of rain evaporation in the bulk model, where r is the ratio of the rain evaporation rate between the bulk and bin simulations and q_r(g kg^{-1}) is the rain mixing ratio. This formula offers a practical fix for the simple bulk scheme in rain evaporation parameterization.

1. Introduction

Mesoscale convective systems (MCSs) are well-organized, long-lived precipitation systems that contribute 30%–70% of the total rainfall over the United States during the warm season (Fritsch et al. 1986). Research into the organization and structure of continental MCSs is important for local precipitation forecasts as well as for understanding the atmospheric energy and water budget (e.g., Houze 2004). In Part I of this paper (Li et al. 2009, hereafter Part I) a summertime MCS over Kansas and Oklahoma [Preliminary Regional Experiment for Storm-Scale Operational and Research Meteorology (PRE-STORM), 10–11 June

Corresponding author address: Xiaowen Li, Code 613.1, NASA GSFC, Greenbelt, MD 20770.
E-mail: xiaowen.li-1@nasa.gov

DOI: 10.1175/2008JAS2647.1

© 2009 American Meteorological Society

1985] was simulated using the 2D Goddard Cumulus Ensemble (GCE) model. Two microphysical schemes—a bulk scheme that prescribes particle size distributions and an explicit bin microphysical scheme that explicitly simulates size distributions—were used with identical environmental conditions, model settings, and initializations in the simulations in Part I. The quasi-steady states (corresponding to the mature stage of the MCS) achieved by the two sets of simulations were compared with each other and also with published observations of the same case. It was shown that model simulations using different microphysical schemes consistently reproduce many features observed during the developing and mature stage of the PRE-STORM MCS, especially in various time-averaged fields.

Significant differences in the bulk and bin scheme simulations are also detailed in Part I. These sensitivities can only be due to assumptions in microphysical processes in the two schemes and the consequent interactions and feedbacks between cloud microphysics and storm dynamics. The focus of this continuing study is to identify key microphysical processes that are responsible for the sensitivities simulated in Part I, using both diagnostic analysis and model sensitivity tests. This is an important step toward improving microphysical schemes and making model simulations converge to observations. In the next section, the difference in the rain evaporation rate calculated by the bulk and bin schemes is identified as the key process responsible for the model sensitivities. In section 3, the role of precipitating ice particles on surface cool pool strength and stratiform region structure are explored. All sensitivity experiments are carried out using the bulk scheme because of its efficiency and simplicity. In section 4, an empirical formula that corrects bulk rain evaporation rate is developed based on the bin simulation. A summary of both microphysical and environmental factors that affect the cool pool–environmental shear balances is presented in section 5, together with a discussion of future works.

2. Surface cool pool and ambient wind shear interactions

a. Description

Interactions between the near-surface cool pool and ambient vertical wind shear and their roles in cell regeneration in MCSs have been investigated by Rotunno et al. (1988) and Weisman and Rotunno (2004), among others. A quantitative criterion, $c/\Delta u$, was defined in Rotunno et al. (1988) and Weisman (1992) to describe the relative strength of the cool pool and ambient wind shear. Here, c indicates the mean cool pool strength generated by the storm:

$$c^2 = 2\int_0^H \left[-g\frac{\Delta\theta}{\theta_0} + 0.61(q_v - q_{v,0}) - q_c - q_r \right] dz - \Delta u_J^2 \tag{1}$$

where q_v, q_c, and q_r are the mixing ratios of water vapor, cloud water, and rainwater, respectively; θ is the potential temperature and $\Delta\theta$ is its deviation from the mean state θ_0; and $\Delta u_J^2 = u_{L,H}^2 - u_{L,0}^2$ represents the contribution of the lower-level rear to front (RTF) flow shear to the cool pool circulation (through its left boundary in our case). Let Δu be the vertical shear of the horizontal wind u in front of (to the right side of) the cool pool. When $c/\Delta u \sim 1$, the horizontal vorticity associated with the wind shear is in near-balance with the vorticity generated by the negative cool pool buoyancy. This balance results in an "optimal state" of leading cell regeneration in the form of a deep, upright convection. When $c/\Delta u > 1$, circulation of the cool pool overwhelms the lower-level wind shear, resulting in a "less-than-optimal, but long-lived state." In this case, the leading cell takes a progressively more upshear tilt as $c/\Delta u$ increases.

Table 1 summarizes some key quantities that corroborate Rotunno et al.'s (1988) theory. All quantities in Table 1 are averages over the last 6 h of simulations, during the quasi-steady stages. The model-prescribed environmental wind shear is $\Delta U_e = 21$ m s^{-1} over a depth of 3.5 km. The average storm-generated cool pool height is about the same (cf. Fig. 11 in Part I). The storm outflow slightly modifies environmental wind shear in front of the MCS, with an average of $\Delta u = 19.1$ m s^{-1} for the bin case and $\Delta u = 18.7$ m s^{-1} for the bulk case. The average $c/\Delta u$ ratio simulated by the bulk scheme is 2.04, compared with 1.01 for the bin case. According to Rotunno et al. (1988), the "less-than-optimal" leading cells simulated in the bulk scheme tilt rearward, as shown in Figs. 6 and 10 in Part I of this paper. As the leading convective core tilts, the lower-level downdraft core deepens and connects with the upper-level downdraft core in front of the leading cell (cf. Fig. 6 in Part I). As a result, the leading cell splits into two, forming a tall, second cell and a shallow, new leading cell. A multicell "strong evolution" storm then occurs in the bulk simulation. In the bin scheme, the $c/\Delta u$ ratio is close to unity, resulting in a "near optimal" balance. Here, a more upright leading updraft core dominates the convective region without cell splitting (cf. Fig. 7 in Part I). The air mass near the ground rises through a relatively deep convective core until it loses most of its buoyancy and detrains at the top of the cell.

TABLE 1. Statistics of the simulated MCSs for the control bulk and bin scheme and the sensitivity tests with the bulk scheme. The averages are taken from the last 6 h of the 12-h simulation, during the mature stage of the storm. The height of the first cell is defined as the radar echo top of 35 db$Z$. A convective core is a structure with vertical air velocity of more than 1 m s^{-1}; w is the averaged vertical air velocity over all cores.

Case	Avg rain (mm day^{-1})	Stratiform portion (%)	$c/\Delta u$	Height (km) 1st cell	System* speed (m s^{-1})	Core at z = 2 km Size (km)	Core at z = 2 km No.	Core at z = 2 km w (m s^{-1})	Core at z = 6 km Size (km)	Core at z = 6 km No.	Core at z = 6 km w (m s^{-1})
bulk	64.5	6.6	2.04	5.7	3.56	4.6	3.5	3.2	5.4	4.4	3.2
bin	56.9	19.6	1.01	7.1	3.01	4.5	1.1	5.2	6.8	1.5	7.7
evap_r0.8	69.8	6.4	1.82	5.9	3.47	4.6	3.7	3.1	5.6	4.3	3.5
evap_r0.5	71.7	5.1	1.23	9.0	2.31	4.4	4.0	3.0	5.4	4.2	4.1
evap_r0.25	42.0	7.4	n/a**	9.6	1.94	3.4	2.3	2.4	4.5	3.2	4.0
evap_c0.4	64.9	6.5	1.97	5.7	3.52	4.4	3.8	3.1	5.3	4.5	3.1
hail_snow_con	57.8	22.1	1.47	6.5	3.66	5.0	3.3	3.3	4.7	3.8	4.2
hail_snow_agg	56.2	19.6	1.48	6.7	3.52	4.9	3.6	3.1	4.5	3.8	4.4
"graupel"	59.7	12.4	1.51	7.8	3.06	3.5	2.3	4.5	3.5	5.0	3.9
graupel_snow_con	58.4	17.6	1.53	7.5	3.43	3.6	2.0	4.8	3.7	4.2	4.4
evap_fitq	72.3	8.5	1.77	6.3	3.56	4.5	4.1	3.2	5.9	4.5	3.6
graupel_s_fitq	60.5	26.4	1.79	7.4	3.33	3.5	2.4	4.5	3.8	4.2	4.2

* The system speed is domain relative. A constant of 12 m s^{-1} needs to be added for the ground relative system speed.

** In this case $c/\Delta u$ is negative because the near surface wind in front of the system is penetrating the convection, contributing to the negative vorticity at the rear edge of the cool pool.

At the same time, the leading cell propagates with the cool pool in a quasi-continuous manner, forming a unicell "weak evolution" storm.

Defining a convective core as a structure with at least 1 m s^{-1} updraft and 1 km in horizontal dimension, Table 1 lists some of the core statistics during the mature stage of the simulations. In the bulk simulation, there are 3.5 cores at 2 km and 5.4 cores at 6 km, compared with only 1.1 and 1.5 cores in the bin simulation. Furthermore, the air rising in the unicell mode can realize its full buoyancy without being interrupted by cell splitting. As a result, the updraft cores simulated by the bin model are stronger than the bulk model, especially at the upper levels. For example, at z = 6 km, the mean vertical velocity inside the updraft cores is 3.2 m s^{-1} for the bulk case compared with 7.7 m s^{-1} for the bin case. The maximum vertical air velocity simulated by the bin scheme is consistently higher than the bulk scheme (cf. Fig. 5 in Part I). The stronger cool pool strength simulated in the bulk scheme also results in a faster-propagating squall system (Rotunno et al. 1988), with a domain-relative propagation speed of 3.47 m s^{-1}, compared with 3.01 m s^{-1} in the bin simulation. Despite the many differences in cell regenerations and updraft core structures, the mean horizontal wind, total heating profile, and mean temperature and pressure structure are very similar between the two simulations.

b. Evaporation diagnoses

Many previous CRM simulations varied the strengths of the wind shear to change the balance between the storm-generated cool pool and the environmental wind shear. For example, Weisman et al. (1988), Fovell and Ogura (1989), Ferrier et al. (1996), and Weisman and Rotunno (2004) all simulated less upshear-tilting convective cells with increasing low-level wind shear. In 3D simulations by Weisman et al. (1988), the low-level wind shear was changed over a wide range. A broad band of weak cells extending behind the leading cell was found in weak wind shear cases, similar to our bulk simulation, whereas convective cells were restricted to a narrow region along the system's leading edge in moderate-to-stronger shear, which is closer to the bin case. Because environmental wind shear is fixed in this study, the sensitivities simulated in Part I can only come from the differences in the simulated cool pool strengths. As the main contributors to the near-surface cool pool, rain and cloud evaporation simulated by the bulk and bin scheme are compared in detail in this section.

In forming the bulk rain evaporation scheme, Kessler (1969) noted—"A constant value of N_0 . . . does some violence to the physics of the evaporation process, since this process actually decreases the relative number of small drops." The shape of rain drop size distribution (DSD) is mainly controlled by the balance of drop coalescence and collisional breakup, especially in convective cores. Theoretical studies show that an equilibrium rain DSD can be achieved near ground level for large rainfall rates, with the large tail forming an exponential shape. When evaporation is included, the large end tends to remain exponential, whereas the number con-

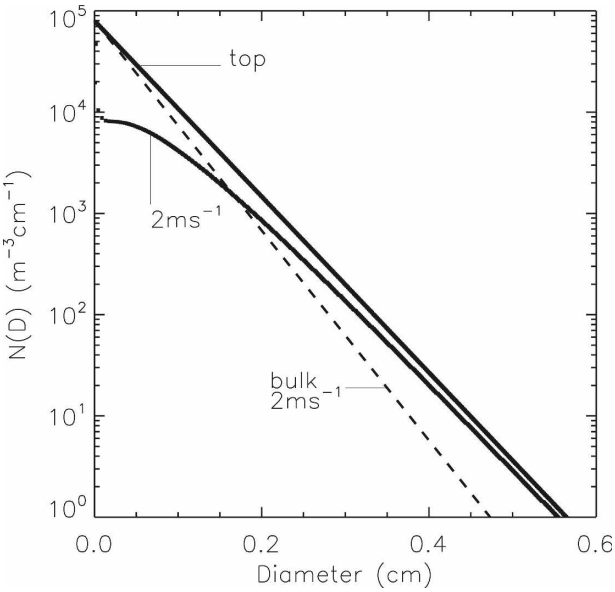

FIG. 1. Rain DSD variations due to evaporation simulated by a rain shaft model. The thick line labeled "top" is the initial exponential DSD. The thick line labeled "2 m s^{-1}" is the DSD of the bin simulation after the drops fall through 4-km depth in a 2 m s^{-1} downdraft. The dashed line is the bulk scheme result.

centrations of small particles are dramatically reduced (e.g., Hu and Srivastava 1995 and Tzivion et al. 1989). A kinematic rain shaft model can be used to illustrate this. This model prescribes the strength of the downdraft and simulates variations of rain DSD using the bulk and bin microphysical schemes, as shown in Fig. 1. The thick straight line in Fig. 1 labeled "top" is the assumed exponential rain DSD at a height of 4 km, where $T = 0°C$ and relative humidity = 100%. The specified initial rain DSD corresponds to a rainfall rate of about 40 mm h^{-1}. The thick line (bin simulation) and the dashed line (bulk simulation) show the rain DSDs after they fall through a distance of 4 km in a downdraft of 2 m s^{-1}. The rate of raindrop evaporation is proportional to its surface area. Small drops evaporate faster than big ones because the former have larger ratios of surface area to volume. This is why the number concentration of small drops decreases faster than that of large drops, resulting in a concave-shaped DSD at the small-size end as shown in Fig. 1. A traditional bulk scheme has only one prognostic variable to represent rain DSD variations. The Kessler (1969) parameterization, as used in the bulk scheme in GCE model, serves to fix the intercept parameter N_0 in the exponential size distribution $N(D) = N_0 \exp(-\Lambda D)$. As a result, the mean raindrop size decreases after evaporation, as opposed to its increase in reality. This leads to an enhanced rain evaporation simulated in the bulk scheme.

In the dynamic frame of GCE simulations in Part I, the bulk scheme also shows enhanced rain evaporation compared with the bin scheme. The rain evaporation rate varies with many factors, such as environmental relative humidity, temperature, pressure, rain mixing ratio, and DSD. Figure 2 isolates the effect of DSD and the relative humidity on rain evaporation by fixing the height at 1 km and taking data for (left) a representative low rain mixing ratio value of 0.5 g kg^{-1} and (right) a high value of 1.5 g kg^{-1}. Each point in Fig. 2 fits these specifications during the 12-h simulation period. The rain evaporation rate should vary linearly with environmental relative humidity provided that all other factors are fixed and the rain DSD is exponential (e.g., Pruppacher and Klett 1997), as shown by the alignment of gray squares along the best-fit lines in Fig. 2 for the bulk simulation. In reality, the faster diminishing of small drops results in smaller evaporation rates. Bin evaporation rates in Fig. 2 generally lie below bulk data under the same environmental condition. The scattering of the bin simulation points indicates variations of rain DSD due to their different growth histories.

In addition to the enhanced rain evaporation at lower levels, cloud droplet evaporation at upper levels is also overestimated by the bulk scheme in which cloud water is assumed to evaporate until the environment is saturated. This is generally true except for when the cloud consists of small amount of large drops due to coagulation, melting, or previous evaporation. Figure 3 is the cloud evaporation rate scatterplot at a height of 5 km. Although the majority of the bin-simulated evaporation (black crosses) occurs in relative humidity above 95%, there are a few large cloud drops existing in an environment as dry as 50%. On the other hand, all the points for the bulk simulation lie above 95% relative humidity, indicating quicker cloud evaporation. Also, the data points with high evaporation rates (above 0.4 day^{-1}) and high relative humidity values occur almost exclusively in the bulk simulation.

Figures 2 and 3 show that because of the simplified evaporation parameterization, the bulk scheme systematically overestimates both rain and cloud evaporation rates. This can also be seen in Fig. 4, which is the instantaneous condensation (positive) and/or evaporation (negative) rates simulated by the (left) bulk and (right) bin schemes. The concurrent vertical air velocity fields are shown in Figs. 6f and 7f in Part I. Consistent with the vertical air velocity structure, condensation rates simulated in the bulk model show multicell structures in the trailing stratiform region, whereas the bin model has a unicell structure, with no condensation in its stratiform region. The shaded area represents an evaporation rate between −0.3 and −0.04 day^{-1}. The shaded area in the bulk simulation is much larger than

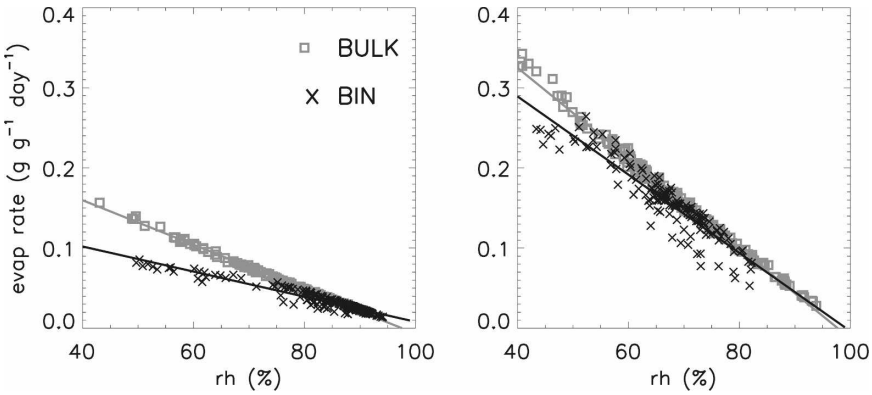

FIG. 2. Variations of rain evaporation rate with environmental relative humidity for rain mixing ratios of (left) 0.5 and (right) 1.5 g kg^{-1} at a height of z = 1 km. Each square (cross) represents one value during the 12-h simulation period for the bulk (bin) model. The straight lines are the least-square linear fits.

that in the bin simulation. Evidence of enhanced cloud evaporation in the bulk scheme can also be found in Fig. 4. For example, the maximum evaporation rate above z = 4 km is -0.77 day^{-1} for the bulk model, compared with -0.37 day^{-1} for the bin model.

c. *Evaporation sensitivity tests*

Diagnostic analyses in section 2b reveal a stronger evaporation rate simulated by the bulk scheme. In this section, sensitivity tests using the bulk scheme are used to support the theory that the strong near-surface cool pool produced by excessive evaporation in the bulk scheme is one of the reasons for the contrasts simulated in Part I. For simplicity, a universal evaporation reduction factor r is applied to the original bulk rain/cloud evaporation parameterization. The mean ratio between the bin and bulk simulated evaporation rate can be used as a rough indication of the possible range of r.

When averaged over the 12-h simulation period, r = 0.61; that is, the rain evaporation rate in the bin scheme is only 61% that of the bulk scheme. This average takes into account both differences in rain DSD assumptions and the positive microphysics–dynamics feedbacks, such that the enhanced rain evaporation increases low-level downdrafts, producing even stronger evaporation. In addition, the stronger near-surface cool pool simulated in the bulk scheme also increases the upshear tilting of the convective cell and moves the rain shaft away from the updraft core. This may further promote rain evaporation. This simple average includes all these feedbacks and is larger than the actual ratio r generated by the rain DSD assumption alone.

To isolate microphysical factors, all available evaporation rates recorded in a 3-min interval are binned according to heights, rain mixing ratio, and environmental relative humidity. An average evaporation rate is then calculated at each bin. Figure 5 shows an example of changes of rain evaporation rate with mixing ratio and relative humidity at z = 1 km. Consistent with previous results (e.g., Figs. 1 and 2), the bulk rain

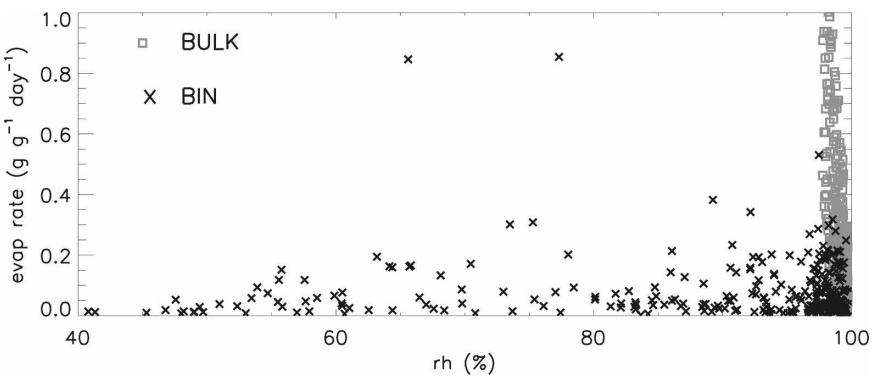

FIG. 3. Variations of cloud evaporation rate with environmental relative humidity at z = 5 km for all cloud mixing ratio values. Squares (crosses) are for the bulk (bin) scheme.

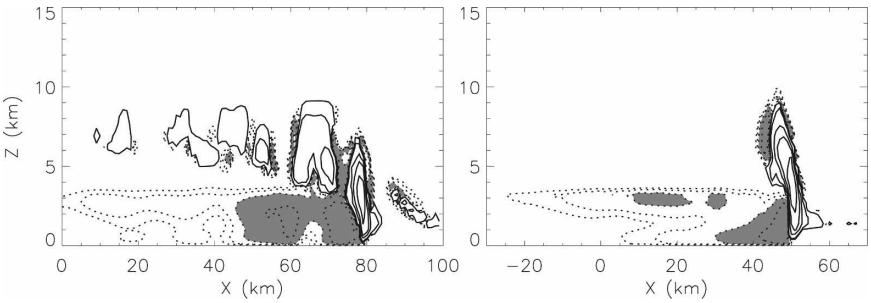

FIG. 4. Instantaneous condensation–evaporation rate field simulated by the (left) bulk and (right) bin scheme at t = 627 min. The contour levels are −0.3, −0.1, −0.04, −0.02, −0.01, 0.01, 0.1, 0.5, 1, and 2 g g^{-1} day^{-1}, with the negative values (evaporation) shown by dashed lines. The shaded area is between the values of −0.3 and −0.04 g g^{-1} day^{-1}.

evaporation rate is always higher than the bin scheme for a wide range of relative humidity and mixing ratios. Contour lines in the bin simulation orient more vertically compared with the bulk simulation, especially when the rain mixing ratio is small and the relative humidity is low. This indicates that as the environmental relative humidity decreases, the enhancement of rain evaporation rate is less steep for the bin simulation because of the loss of small drops. When the ratio r is calculated for each bin, the evaporation enhancement due to microphysics–dynamics interactions is removed. The ratio r averaged over different levels is 0.83. Note that r = 0.83 does not consider the underestimated mean fall velocity of raindrops in the bulk scheme, which allows for longer sedimentation time and may further enhance rain evaporation.

Based on the diagnostic analysis, r = 0.8 is used for the first sensitivity test, evap_r0.8. Some key characteristics of the test evap_r0.8 are listed in Table 1. Reducing rain evaporation rate by 20% in the bulk scheme results in a slightly weaker near-surface cool pool. The average value of $c/\Delta u$ decreases from 2.04 in the control bulk simulation to 1.82. The average height of the 30-dBZ radar echo top of the first cell is used to indicate the extent of the upshear tilting: the higher the leading cell, the less tilting. Weaker cooling in test evap_r0.8 produces a more upright leading convection and a slower propagating system compared with the control bulk run, all consistent with Rotunno et al. (1988). The system simulated in evap_r0.8 remains a multicell storm with a strong evolution mode, the same as the control bulk simulation. The average updraft core sizes and numbers at both z = 2- and 6-km levels are similar between evap_r0.8 and the bulk simulation. Figures 6a and 6b show the instantaneous radar reflectivity at t = 12 h, simulated by evap_r0.8, and the surface rainfall time–domain plot. Comparing Figs. 6a and 6b with Figs. 1 and 3 in Part I, we find that the test evap_r0.8 remains essentially similar to the control bulk simulations, with the cell structure extending well into the stratiform region (Fig. 6a) and distinctive surface rainfall streaks (Fig. 6b).

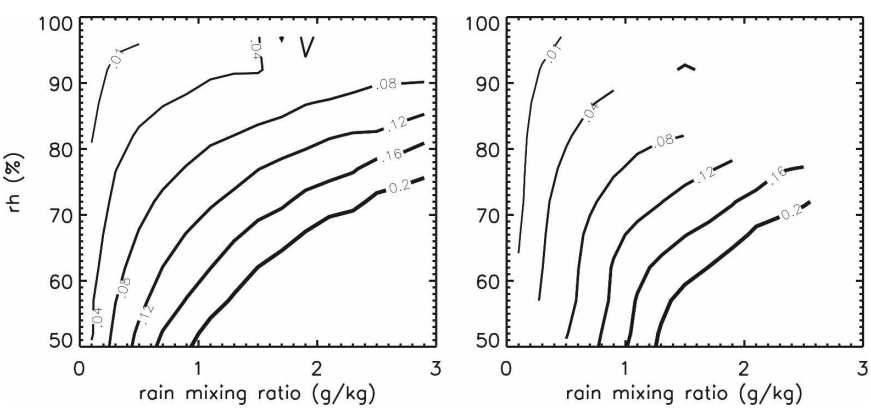

FIG. 5. Variations of the average rain evaporation rate with rain mixing ratio and environmental relative humidity at z = 1 km for the (left) bulk and (right) bin scheme. The contour levels are at 0.01, 0.04, 0.08, 0.12, 0.16, and 0.2 g g^{-1} day^{-1}, with thicker lines for larger values.

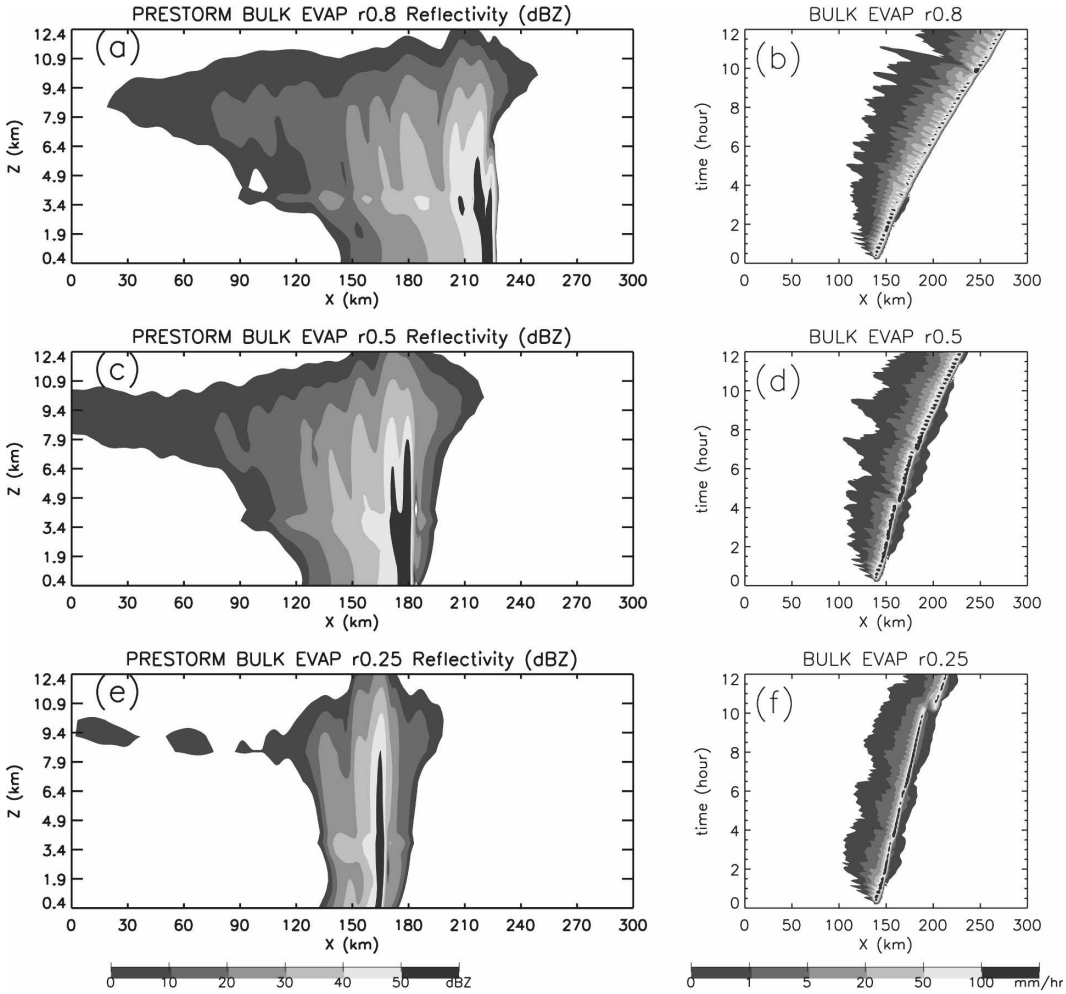

FIG. 6. (left) Simulated instantaneous radar reflectivity (dBZ) at t = 12 h and (right) surface rainfall time–domain diagram for three sensitivity tests using the bulk scheme: (a), (b) evap_r0.8, in which the rain evaporation rate is reduced by a factor of 0.8; (c), (d) test evap_r0.5, in which the rain evaporation rate is reduced by half; and (e), (f) evap_r0.25, in which the rain evaporation rate is reduced by a factor of 0.25.

The test evap_r0.8 shows that reducing rain evaporation rate in the bulk model by the average ratio results in sensitivities in the correct direction, but to a much lesser degree compared with the contrasts simulated in Part I. To further test the effect of the balance between the surface cool pool and wind shear, two additional sensitivity tests using r = 0.5 (evap_r0.5) and r = 0.25 (evap_r0.25) were performed, as shown in Table 1 and Figs. 6c–f. When the rain evaporation rate is cut in half in the bulk scheme, both the stratiform rain portion and its area decrease compared to the control bulk experiment. The average surface rain area during the mature stage (after 6 h) decreases from ~80 km for the bulk control experiment to about 70 km for test evap_r0.8 and ~60 km for test evap_r0.5. The test evap_r0.5 still produces an essentially multicellular storm, as shown by the high-reflectivity cells embedded in the stratiform region in Fig. 6c and the high rainfall rate streaks in Fig. 6d. On the other hand, the temporal variations of the leading cell regeneration become weaker. In Fig. 7, the new leading cell remains connected to the deep cell, which would become the second cell, for much of the cell regeneration cycle. The leading updraft core, therefore, remains the deepest with one exception at t = 639 min, at which point the second cell remains very close to the leading cell. Figure 7 indicates that the mode of evolution for evap_r0.5 is in between the weak evolution and the strong evolution defined in Foote and Frank (1983). These indicate that the strong evolution and weak evolution modes are at the two ends of a spectrum of temporal variations regarding cell regenerations.

The simulation evap_r0.25 reduces the rain evaporation rate to one quarter of its bulk scheme value. Com-

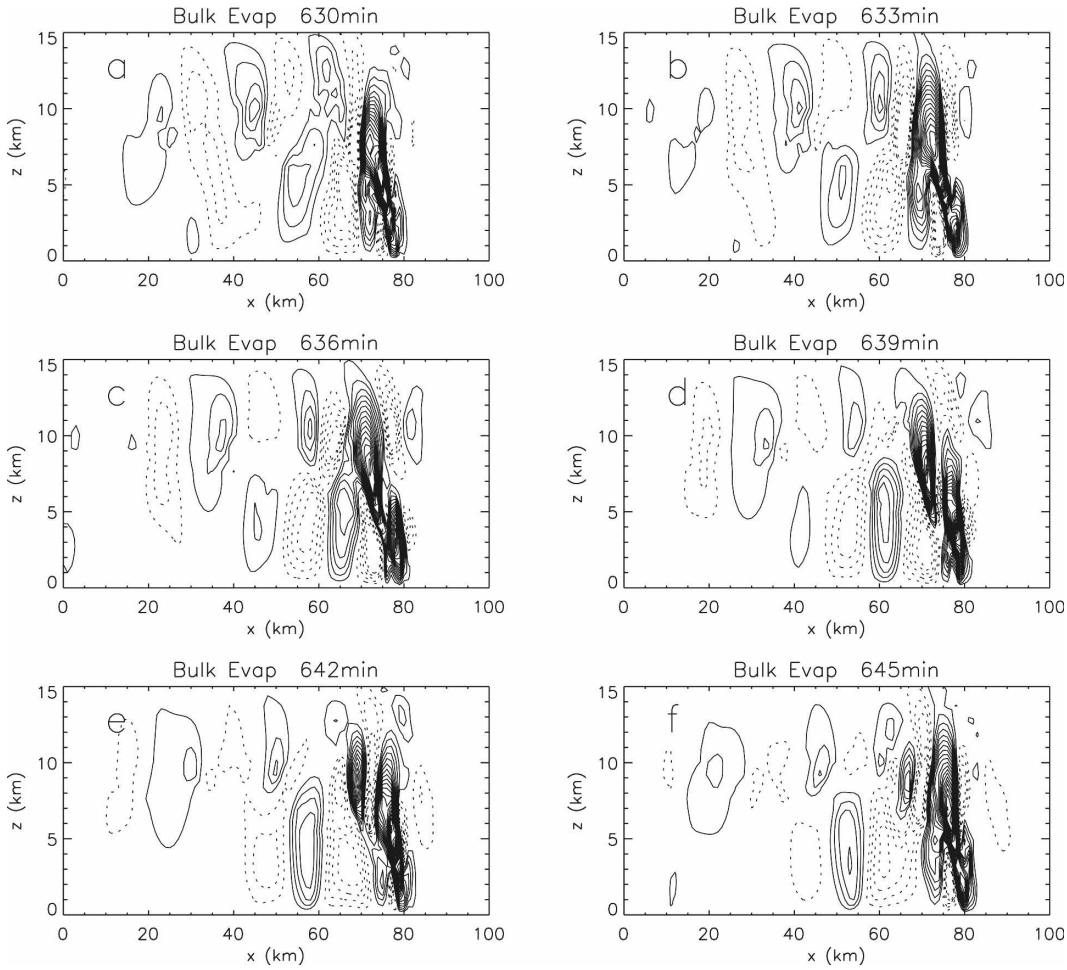

FIG. 7. Leading cell regeneration cycle shown in the instantaneous vertical air velocity fields simulated by evap_r0.5. The frames are at 3-min intervals for 15 min. The contour interval is 1 m s^{-1} with positive velocities having solid lines and negative velocities having dashed lines.

paring the characteristics listed in Table 1, a clear trend of increasing dominance of the near-surface wind shear over the cool pool strength is found when the rain evaporation rate is progressively reduced. The $c/\Delta u$ value decreases monotonically from 2.04 for the control bulk case to 1.23 for evap_r0.5. The 30-dBZ radar echo top height of the leading cell increases as the cool pool strength decreases, indicating a trend of more upright leading cell as suggested in Rotunno et al. (1988). The system propagation speed also decreases. In terms of the temporal variation mode, the test evap_r0.25 produces a weak evolution storm during the mature stage, as shown in Fig. 8. The upright leading cell in Fig. 8 remains a steady feature through the 15-min period. The same conclusion can also be drawn from the updraft core statistics listed in Table 1. Notice that the core size and average core strength at $z = 2$ km are relatively small in evap_r0.25, resulting from smaller and weaker minor updraft cores.

The horizontal wind and pressure perturbation fields for the three sensitivity tests are plotted in Fig. 9. In the horizontal wind fields (Figs. 9a, 9c, and 9e), the strength of the front to rear outflow at the mid-to-upper levels reduces significantly with r. The rearward transport of ice particles by this flow, which is the major contributor to the stratiform rain, is also reduced. The lower-level RTF inflow weakens because of the reduced stratiform area and rain evaporation, and its downward bending near the leading convection becomes weaker. In the extreme case in evap_r0.25, the RTF inflow no longer touches the ground. As a result, part of the near-surface inflow goes through the system without contributing to the leading updraft core, causing a significant weakening of the system strength (see, e.g., the rainfall rates shown in Table 1). In the pressure perturbation fields (Figs. 9b, 9d, and 9f), the narrow surface high generated by the cool pool becomes weaker as the rain evaporation rate is reduced. The midlevel meso-low also be-

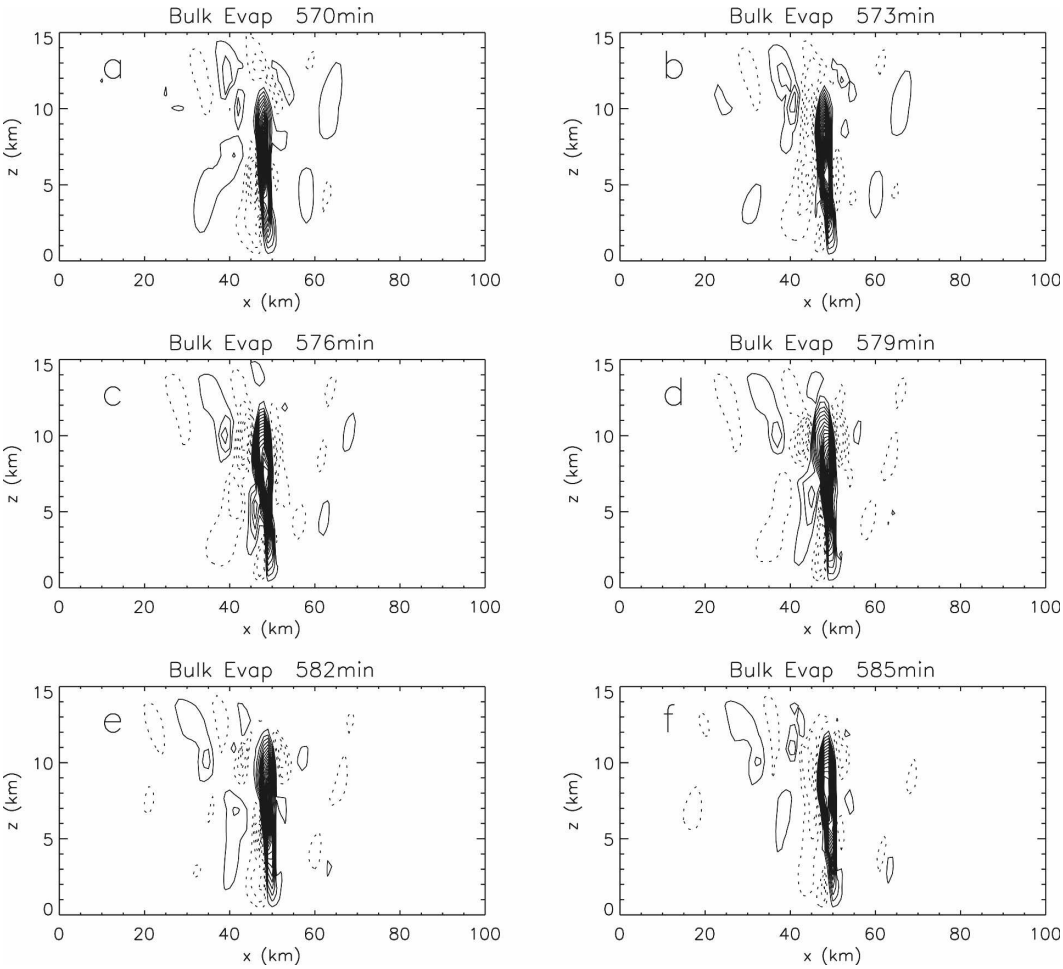

FIG. 8. As in Fig. 7, but for evap_r0.25.

comes weaker and smaller as the stratiform region and the buoyant air associated with it reduce. For the extreme case evap_r0.2, the midlevel low is confined near the leading cell.

In addition to rain evaporation, the diagnostic study in section 2b also indicates overestimated cloud evaporation in the bulk scheme. A sensitivity test that reduces cloud evaporation rate is carried out to determine its effect on storm structures. Test evap_c0.4 uses a mean reduction factor of $r_c = 0.4$, which is derived from the simulations. Key statistics of the test evap_c0.4 are listed in Table 1. Comparisons of evap_c0.4 with the original bulk run indicate that the storm structure is not sensitive to the cloud evaporation rate. Additional sensitivity tests (not shown here) that reduce rain and cloud evaporation rate simultaneously tend to make the minor updraft cores weaker at upper levels when the storm approaches a unicell structure. However, general storm structures and rainfall characteristics do not change significantly when the cloud evaporation rate is reduced in the bulk model.

Sensitivity tests in this section support the hypothesis that artificially enhanced rain evaporation in the bulk scheme is partially responsible for the different spatial and temporal variation modes simulated by the bulk and bin schemes. However, a unicell, weak evolution mode, as simulated in the bin scheme, is only achieved by dramatically reducing rain evaporation rate to a quarter of its original bulk value. This reduction ratio is much smaller than the average ratios of 0.83 (microphysics only) and 0.61 (microphysics and their interactions with dynamics) derived from the control experiments. Furthermore, even as evap_r0.25 produces a unicell, weak evolution leading convection, it further exacerbates the differences in the stratiform region between the two schemes. The stratiform area is reduced as the simulated storm changes from a multicell, strong evolution mode to a unicell, weak evolution mode, as

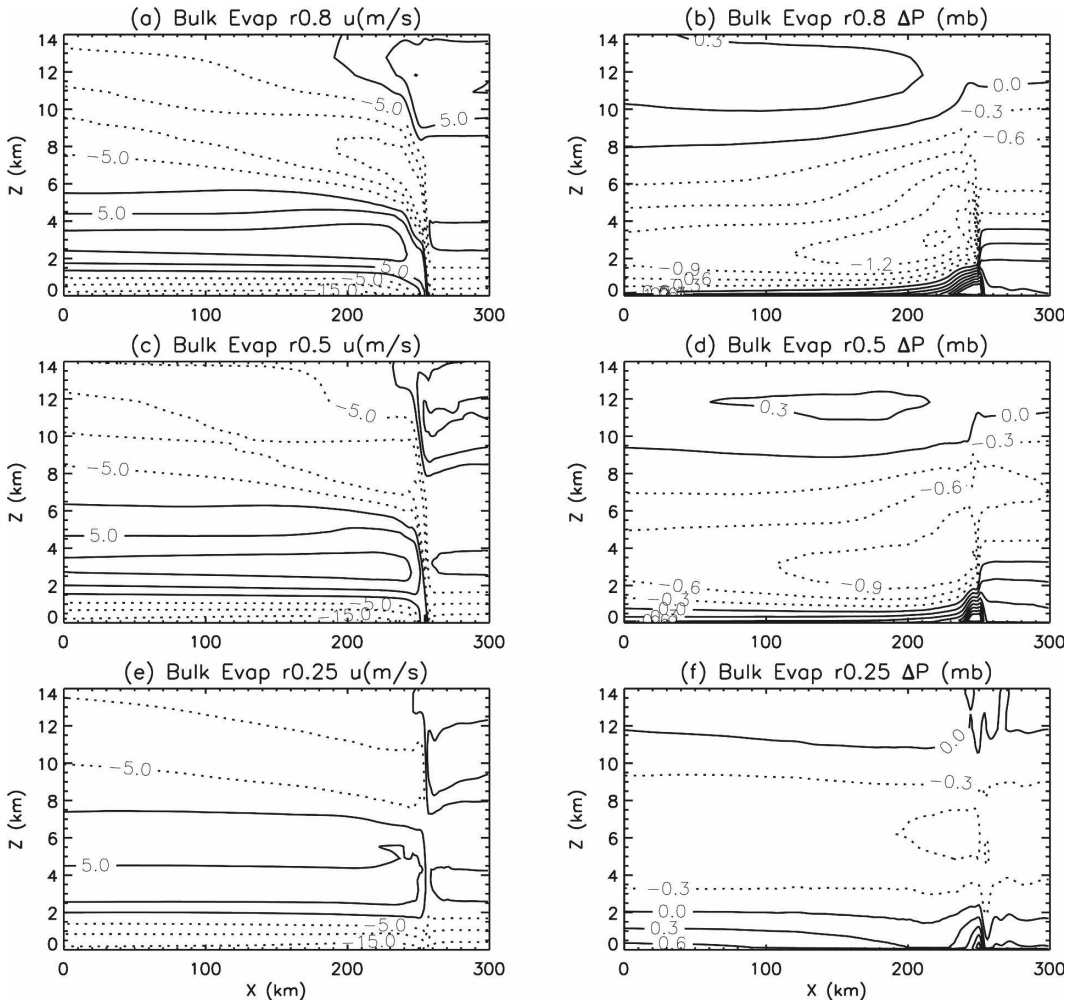

FIG. 9. (left) Time-averaged horizontal wind and (right) pressure perturbation for bulk scheme sensitivity tests (a), (b) evap_r0.8, (c), (d) evap_r0.5, and (e), (f) evap_r0.25 during their mature stages (6–12 h). Dashed lines represent negative values. The contour interval is 5 m s^{-1} for the wind fields and 0.3 mb for the pressure perturbation fields.

shown in Fig. 6. In the next section, the role of precipitable ice particles in shaping the storm structure and dynamics, especially in the stratiform region, is investigated.

3. Precipitable ice particles and their role in stratiform region

The stratiform region in the bulk simulation in Part I is made primarily of remnants of the previous leading cells. When the rain evaporation rate is reduced, the number of convective cells decreases, causing the stratiform area to shrink (Fig. 6). To form a large stratiform area without relying on the rearward-propagating convective cells, as simulated by the bin scheme, the amount of rearward transport of ice particles needs to be increased (e.g., Fovell and Ogura 1988). There are two ways of increasing rearward ice particle transport: by changing the partitioning of the precipitable ice particles (e.g., Thompson et al. 2004; Lang et al. 2007) or by changing the fall velocity and/or density of the ice particles. Both of these will be explored using the bulk scheme.

a. Partitioning of ice particles

Snow and hail are the two precipitable ice phase particles in the Lin et al. (1983) scheme. In this section, the partitioning of the snow and hail in the original bulk scheme is modified in an attempt to produce more slow-falling snow at the expense of fast-falling hail. Also, the rainfall rate in the convective region reduces with less hail production. Because the rain evaporation in the downdraft region immediately behind the leading

convection contributes significantly to the surface cool pool, less hail production also weakens the cool pool and results in a more upright leading cell, which in turn reduces the rain evaporation even more. This positive feedback mechanism will make the bulk scheme more sensitive to the reduction of rain evaporation.

The hail growth equation in the original bulk scheme is (Lin et al. 1983):

$$P = P_{\mathrm{AUT}} + P_{\mathrm{FR}} + P_{\mathrm{DRY}} + P_{\mathrm{SACR}}(1 - \delta_2) + P_{\mathrm{RACS}}(1 - \delta_2) + P_{\mathrm{RACI}}(1 - \delta_3) + P_{\mathrm{IACR}}(1 - \delta_3) - P_{\mathrm{SUB}}(1 - \delta_1) + P_{\mathrm{HACW}} + P_{\mathrm{HACI}} + P_{\mathrm{HACR}} + P_{\mathrm{HACS}}, \quad (2)$$

in which, for temperatures below freezing,

$$\delta_1 = \begin{cases} 1, & \text{when either cloud water or cloud ice exists} \\ 0, & \text{otherwise} \end{cases}$$

$$\delta_2 = \begin{cases} 1, & \text{for both rain and snow mixing ratio less than 0.1 g kg}^{-1} \\ 0, & \text{otherwise} \end{cases}$$

$$\delta_3 = \begin{cases} 1, & \text{for rain mixing ratio less than 0.1 g kg}^{-1} \\ 0, & \text{otherwise.} \end{cases}$$

Here, P_{AUT} is the autoconversion of snow to hail, P_{FR} is the freezing of rain, P_{SACR} is the accretion of rain by snow, P_{RACS} is the accretion of snow by rain, P_{RACI} is the accretion of ice by rain, P_{IACR} is the accretion of rain by ice, P_{SUB} is the sublimation of hail [the only sink term in Eq. (2)], P_{HACW} is the accretion of cloud water by hail, P_{HACI} is the accretion of ice by hail, P_{HACR} is the accretion of rain by hail, and P_{HACS} is the accretion of snow by hail. Two sensitivity tests that reduce the hail production terms (and therefore enhance the snow amount) are carried out in this section: the test hail_snow_con does a conservative tuning in Eq. (2) and the test hail_snow_agg does an aggressive, somewhat unrealistic tuning.

The test hail_snow_con removes the terms P_{AUT}, P_{HACI}, and P_{HACS} in Eq. (2). In other words, there is no autoconversion or dry growth of hail. The efficiencies of high-density hail collecting ice are quite small, 0.1 in the original scheme. They are set to be 0 in the test hail_snow_con. These assumptions are believed to be reasonable and they form the conservative version of the sensitivity test. In addition to the tunings in hail_snow_con, the more aggressive tunings in hail_snow_agg assume 0.5, instead of 1, for the collection coefficient of the ice phase and water phase particles in the terms P_{SACR}, P_{RACS}, P_{RACI}, P_{IACR}, P_{HACW}, and P_{HACR}. Furthermore, the mixing ratio threshold in δ_2 and δ_3 is raised from 0.1 to 1 g kg^{-1}, making it much easier to form snow than hail when ice phase particles collide with water phase particles. The rate of raindrop freezing is also reduced by about two orders of magnitude by using the experimental parameter of rain freezing from distilled water instead of from rainwater (Pruppacher and Klett 1997). These tunings are considered unrealistic and they form the aggressive sensitivity test hail_snow_agg. All sensitivity tests in this section used a reduction factor of $r = 0.8$ for rain evaporation.

Figure 10 illustrates the results from this set of sensitivity tests. The instantaneous radar reflectivity and the domain-average hydrometeor profiles are plotted for the original bulk scheme (Figs. 10a and 10b), hail_snow_con (Figs. 10c and 10d), and hail_snow_agg (Figs. 10e and 10f). A trend of increasing snow amount and decreasing hail amount is obvious in the hydrometeor profiles at the right column. With more snow transported rearward, the stratiform area becomes wider. In the meantime, the leading convection is increasingly taller and more upright. The stratiform rain makes up 22.1% and 19.6% of the total rainfall for the test hail_snow_con and hail_snow_agg, respectively, compared with only 6.6% for the original bulk scheme. These results also show that unrealistic, aggressive tuning as in hail_snow_agg is probably not necessary. Both conservative and aggressive tuning show storm structures and characteristics similar to those shown in Fig. 10 and Table 1, although the test hail_snow_agg does have more snow aloft and a wider stratiform region, and its temporal variation mode is weaker than that of hail_snow_con.

There are still differences in the tuned bulk and the bin simulation, the most obvious of which is that even with the aggressive tuning, the resulting storm is still a multicell system, in contrast to a unicell system simulated by the bin model. Figure 11 shows a typical cell regeneration cycle simulated by hail_snow_agg for a 15-min time period. There are generally three to four convective cells at any level over the time period. In terms of the temporal variation, the test hail_snow_agg

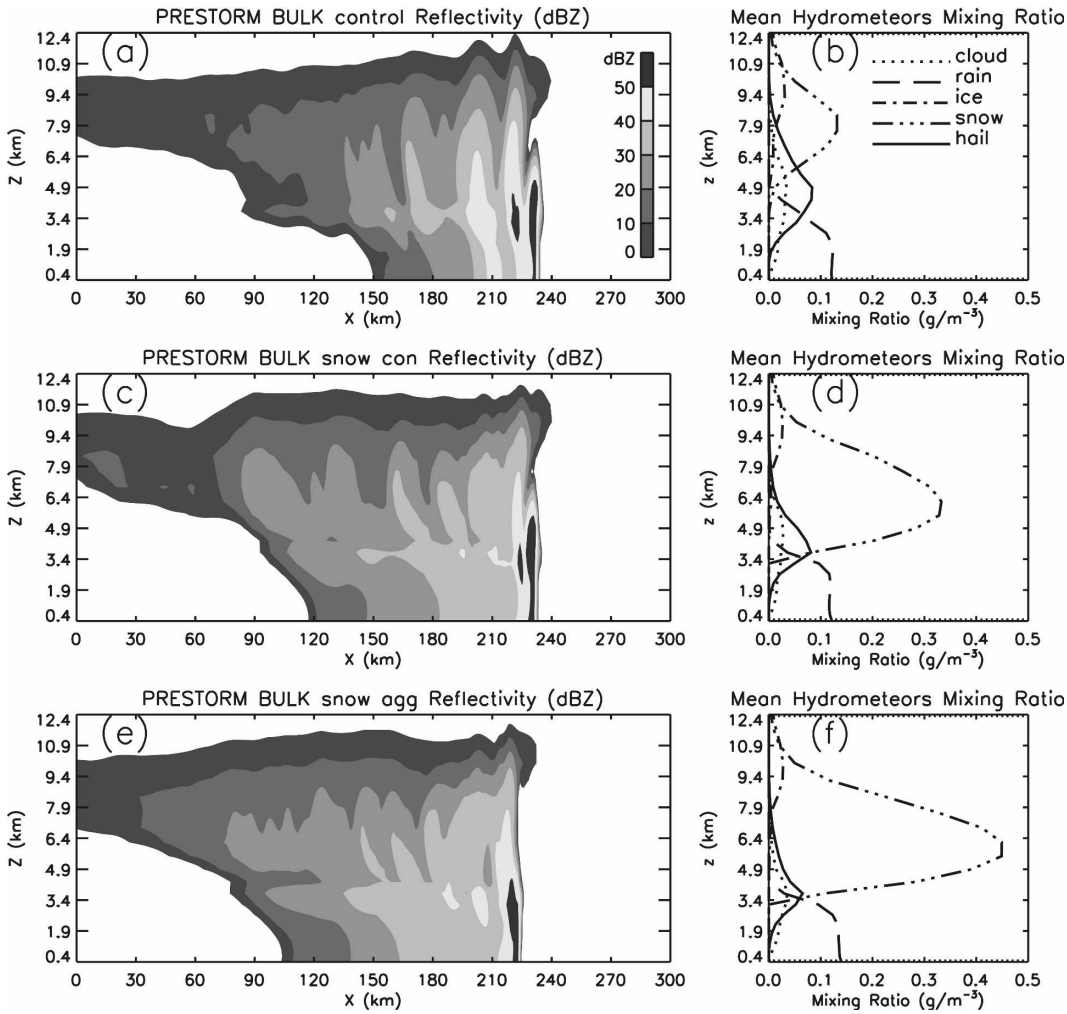

FIG. 10. (left) Radar reflectivity and (right) domain-averaged mixing ratio profiles of different hydrometeors at $t = 12$ h for the bulk scheme sensitivity tests on the partition of precipitable ice particles: (a), (b) the original bulk scheme; (c), (d) the sensitivity test using conservative tuning to produce more snow at the expense of hail (hail_snow_con;); (e), (f) the test using aggressive tuning (hail_snow_agg).

produces a storm that is in between a typical strong evolution mode and a weak evolution mode, similar to evap_r0.5 shown in Fig. 7. However, the respective surface rainfall distribution and radar reflectivity structure in evap_r0.5 and hail_snow_agg are quite different (cf. Figs 6c and 10e). Stratiform rain contributes to 19.6% of the total rainfall in hail_snow_agg, compared with only 5.1% in evap_r0.5. Comparing these two cases, one can find important feedbacks of the trailing stratiform region on storm dynamics and structure (e.g., Lafore and Moncreiff 1989; Weisman 1992). First, transporting precipitable ice particles to the trailing stratiform region reduces rain evaporation rate in the convective region. However, this is partially compensated for by the enhancement of the cold RTF inflow that strengthens the cool pool. Second, enhanced wind shear in the RTF inflow acts to reduce the negative vorticity generated by the cool pool. With a more extensive stratiform region during the mature stage, test hail_snow_agg maintains a stronger vertical shear in its RTF inflow, as shown in Fig. 12a, compared to evap_r0.5 (Fig. 9c). This is why evap_r0.5 and hail_snow_agg have similar cell propagation modes but display very different storm structures, especially in the stratiform region.

Both sensitivity tests in this section still show a smaller stratiform area compared with both the bin simulation and observations. Furthermore, the storms retain their multicellular structure, although their temporal variation modes shift toward a weak evolution. Further reducing the snow particles' fall velocity by tuning either its size distribution parameter or its fall

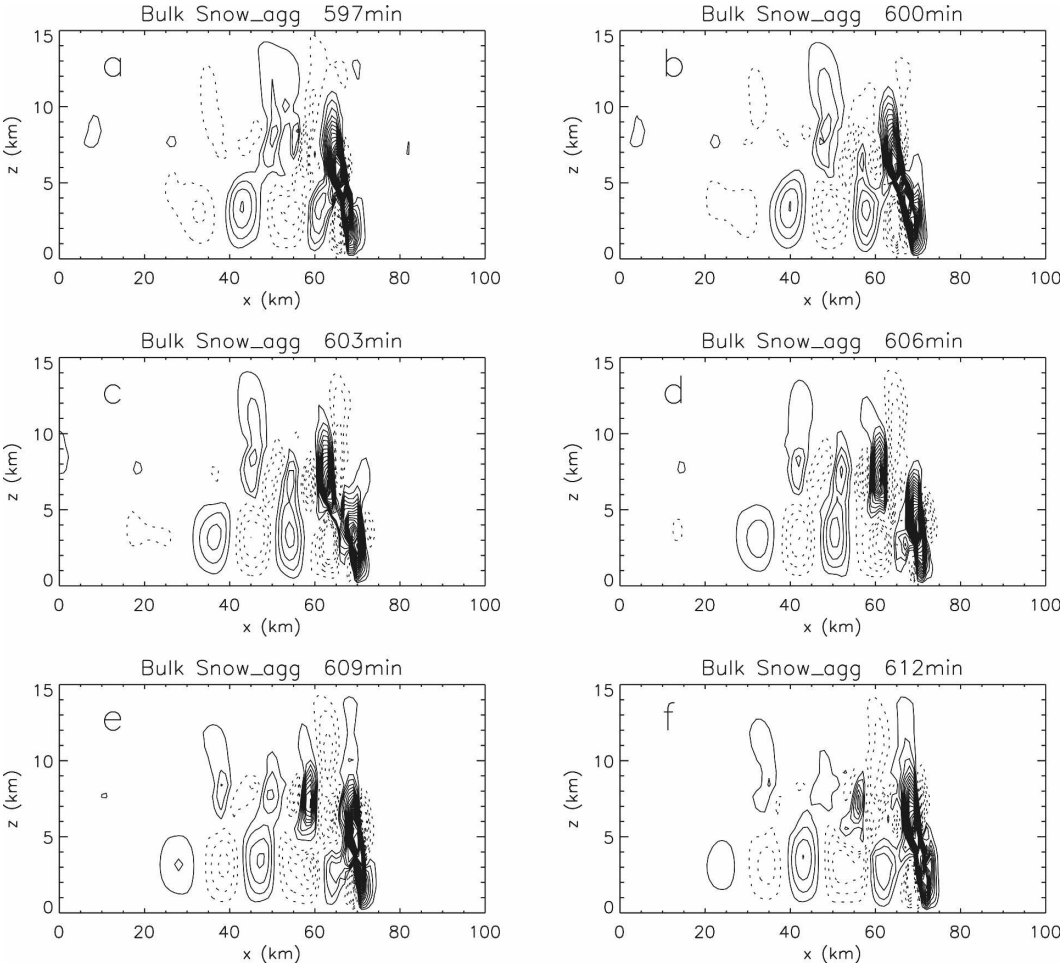

FIG. 11. As in Fig. 7, but for hail_snow_agg.

velocity parameter does not change the results significantly. Sensitivity tests in the next section reduce the fall velocity of the fast-falling ice species by replacing the high-density hail particles (assumed to be 0.9 g cm^{-3} in the original bulk scheme) by low-density graupel (0.4 g cm^{-3}).

b. *Fall velocity of ice particles*

Rutledge and Hobbs (1984, hereafter RH84) developed a bulk microphysical scheme similar to Lin et al. (1983) in which they considered graupel instead of hail as the end product of cloud and rain freezing and col-

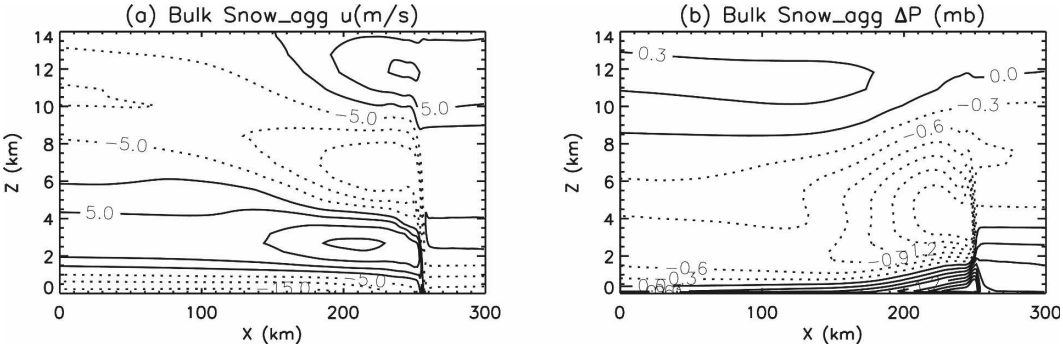

FIG. 12. As in Fig. 9, but for hail_snow_agg.

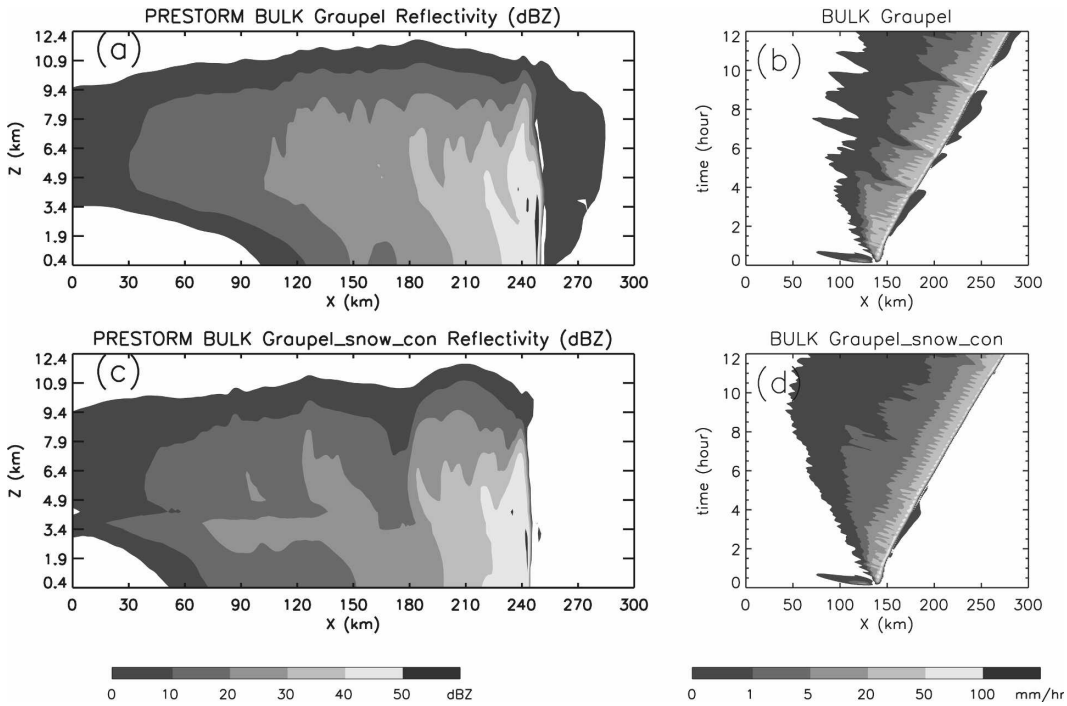

FIG. 13. As in Fig. 6, but for the sensitivity tests (a), (b) "graupel" and (c), (d) graupel_snow_con.

lection. Previous GCE model simulations indicate that the Lin et al. (1983) scheme with high-density, fast-falling hail represents strong continental convection better, whereas the RH84 scheme produces better results in simulating maritime storms where the updraft is weaker (McCumber et al. 1991). Although the PRESTORM case is a strong continental squall line, and hail has been observed at least during the developing stage of the squall (Johnson and Hamilton 1988), using the RH84 scheme in sensitivity tests in this section is still meaningful in establishing the importance of fall velocities of precipitable ice particles on the storm structure and dynamics.

Two sensitivity tests using the RH84 scheme with slow-falling graupel are carried out in this section. The test "graupel" replaces the fast-falling hail with graupel. The snow terminal fall velocity is also reduced by reducing its mean size. The test graupel_snow_con changes the partitioning between graupel and snow in the same way as in hail_snow_con, in addition to the tunings in the test "graupel." Figure 13 shows the simulated radar reflectivity at $t = 12$ h and the surface rainfall time–domain plots. Both tests produce much wider stratiform rain compared with even the aggressively tuned hail_snow_agg test. Compared with the bin simulation, the test "graupel" still falls short of the amount and size of the stratiform rain. "Graupel" produces 12.4% of stratiform rain among its total rainfall compared with 19.6% for the bin simulation. The test graupel_snow_con has 17.6%.

Discrepancies still exist between graupel_snow_con and the bin simulation. For example, the storm retains its multicellular structure compared to the unicell storm simulated in the bin scheme. The convective core number has been reduced to 2 at $z = 2$ km in graupel_snow_con, but remains 4.2 at $z = 6$ km. This is because in this case, the secondary cells are much weaker compared with the primary cell and the majority of them remain aloft in the stratiform region. Consistently, the temporal variation mode of test graupel_snow_con is weaker compared with the other bulk simulations but is still stronger than the bin simulation. Figure 14 shows the horizontal wind and pressure perturbation fields for the tests "graupel" and graupel_snow_con. Consistent with the experiments in section 3a, the simulated storm with more extensive trailing stratiform region has stronger RTF inflow and the front to rear outflow right above it. The low-pressure center in the midlevel also becomes deeper and wider. Comparing Fig. 14c with the bin simulation in Fig. 4b in Part I, one can see that both the RTF inflow and the front to rear outflow are slightly weaker in graupel_snow_con. Comparison of Fig. 14d here and Fig. 11e in Part I also shows a similar strength but less extensive midlevel low pressure center

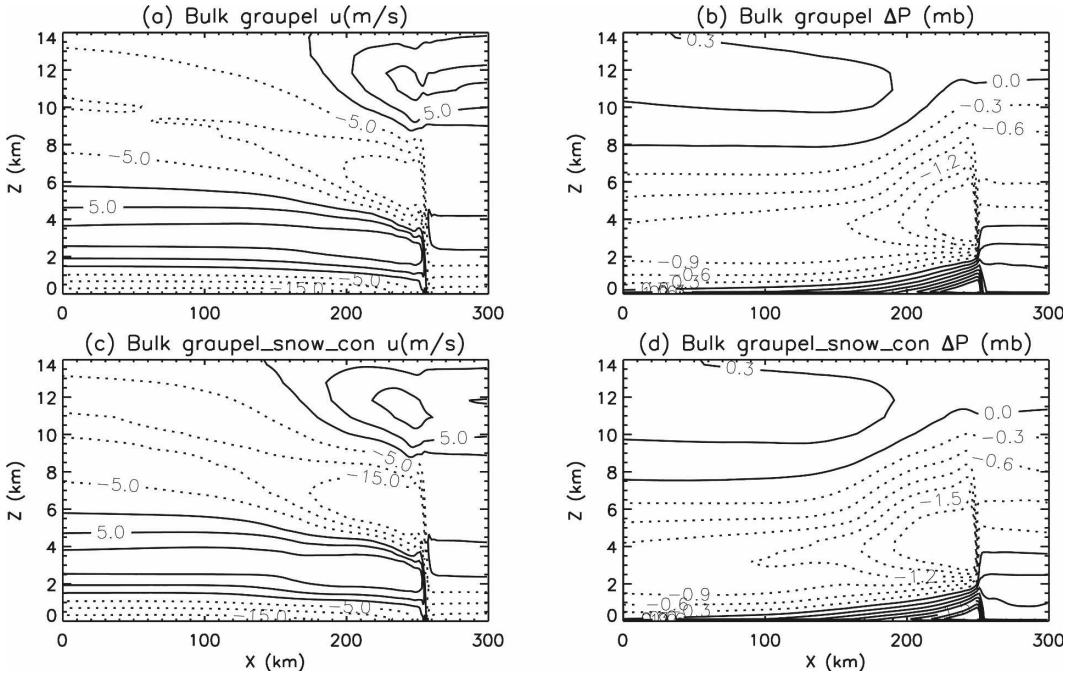

FIG. 14. As in Fig. 9, but for (a), (b) "graupel" and (c), (d) graupel_snow_con.

in graupel_snow_con, indicating a more extensive diabetic heating in the stratiform region in the bin simulation.

Sensitivity tests in this and the previous section show a clear trend of increasing stratiform region when fall velocities of precipitable ice particles are reduced. Other characteristics, such as mean horizontal flow, temperature, pressure perturbation, and spatial and temporal variation modes also approach the bin simulation. However, none of these sensitivity tests produces a unicell, weak evolution system despite the clear trend toward that direction. Further improvements in ice phase microphysics in both the bulk and bin scheme are needed to make them converge to the observations.

4. Correction factor for the bulk rain evaporation

Previous sections have used a mean factor r to reduce bulk rain evaporation rate for idealized sensitivity tests. Here an empirical correction factor is developed to improve rain evaporation as represented in bulk microphysical parameterizations. Both environmental factors and rain DSDs affect rain evaporation rates. A bulk cloud model simulates environmental conditions but must make assumptions about rain DSDs. The ratio between the bulk- and bin-simulated rain evaporation indicates deviations of these assumptions from the bin-simulated rain DSDs. Figure 15 shows variations of the ratio r with (a) rain mixing ratio, (b) environmental relative humidity, and (c) height simulated in the models. The vertical bars represent one standard deviation. Figure 15a shows that varying the rain mixing ratio produces the largest and most consistent variation in r, especially when the rain mixing ratio is low. Here small drops become depleted very fast, leaving only a limited number of large drops, which do not evaporate as effectively. At 0.1 g kg^{-1}, the bulk scheme simulates the evaporation rate 3 times more strongly on average compared with the bin scheme. The ratio decreases monotonically to 1 with increasing rain mixing ratio. At its large end ($q_r > 2.6$ g kg^{-1}), the bin scheme even has a slightly higher rain evaporation rate, indicating the presence of more small particles compared with the exponential size distribution assumed in the bulk scheme for heavy rain rates. In Fig. 15b, the ratio is higher at low relative humidities because the evaporation is faster in drier environments. The ratio increases again at above 90% relative humidity, presumably because these points are mainly located in the stratiform region, where ice aggregation results in a larger raindrop size compared with the convective region (e.g., Rosenfeld and Ulbrich 2003). This exacerbates differences between the bulk and bin schemes. However, the trends with both relative humidity and height are highly uncertain, as shown by the large standard deviation bars in Figs. 15b and 15c. For this reason, only the rain mixing ratio is used to fit an empirical correction factor for r.

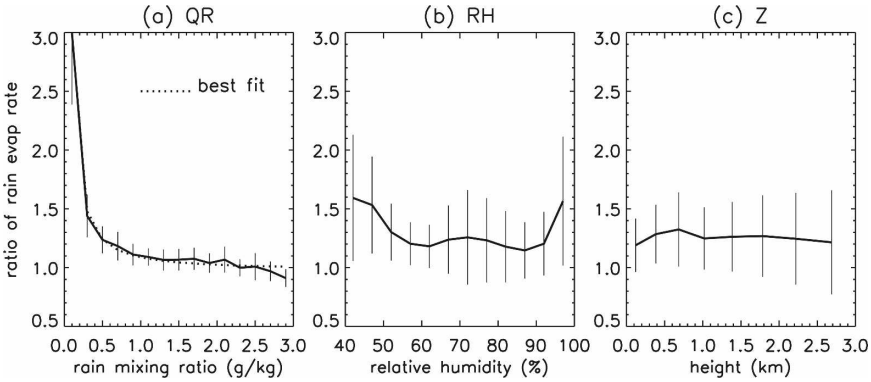

FIG. 15. Variations of rain evaporation rate ratio between the bulk and bin microphysics (r) with (a) rain mixing ratio, (b) relative humidity, and (c) height. The vertical lines indicate one standard deviation. The dotted line in (a) is the best-fit line.

Variations of the ratio r with rain mixing ratio q can be described by the function $r(q_r) = Cq_r^A + B$, where the constants A, B, and C are determined by least squares regression. In this case study, $A = -1.27$, $B = 0.98$, $C = 0.11$, and q_r is in the unit of g kg^{-1}. This best-fit ratio $r(q_r)$ is applied to the same PRE-STORM case simulation in two previously described bulk schemes: the original control bulk scheme and the test graupel_snow_con, in which hail is replaced by graupel and snow production terms are tuned conservatively. Some of the simulated storm characteristics are listed in Table 1 under the case names evap_fitq and graupel_s_fitq. The temporal and spatial variation modes, as well as kinematic structures of the simulated storms, remain very similar to their corresponding tests using the fixed r factor of 0.8 (evap_r0.8 and graupel_s_fitq). One noticeable difference is that when $r(q_r)$ is used, the simulated storms consistently produce more stratiform rain and a wider stratiform area compared with the fixed r approach.

Rapidly increasing computational power is allowing more and more sophisticated microphysical schemes (e.g., multimoment, bin spectral) to be used in atmospheric modeling. However, the simple bulk microphysics schemes remain useful for large-scale (e.g., regional or global cloud-resolving models) and long-time (e.g., climate) modeling. Here the empirical correction factor $r(q_r)$ provides a practical fix for the overestimation of rain evaporation rates in simple bulk microphysical schemes.

5. Summary and discussion

Significant differences in storm structures and temporal variations simulated by two independent microphysical schemes with different complexities prompted the studies detailed in this second part of a two-part paper. The overall goal of this research is to identify mechanisms of these differences and to understand the interactions between cloud microphysics and storm dynamics. It is found that the balance between the storm-generated cool pool and the environmental lower-level wind shear is the key factor that produces the contrasting storm features simulated by the bulk and bin microphysical schemes. Two key processes that affect the strength of the cool pool circulation are the rain evaporation rate and the fall velocities of precipitable ice particles.

The Lin et al. (1983)-type bulk scheme assumes an exponential rain DSD. This assumption artificially increases the portion of small raindrops during evaporation. As a result, the bulk scheme overestimates rain evaporation, which results in a stronger near-surface cool pool compared with the bin simulation. The dominance of the cool pool circulation over the near-surface environmental wind shear is the main reason for the rearward-tilting, multicellular storm structure simulated in the bulk scheme, in contrast to the upright, unicell storm with a weak evolution mode produced by the bin scheme. Sensitivity tests that reduce rain evaporation rate in the bulk scheme are able to produce progressively more upright leading convection as well as weaker and fewer secondary cells. The temporal variations of the leading cell regeneration also become progressively weaker. However, a unicell storm with weak evolution mode is only achieved by dramatically reducing rain evaporation rate to one quarter of its original value. Also, the resulting storm has very little trailing stratiform region.

Further, sensitivity tests that reduce the mean fall velocity of precipitable ice particles—which also affects the cool pool circulation in addition to allowing more

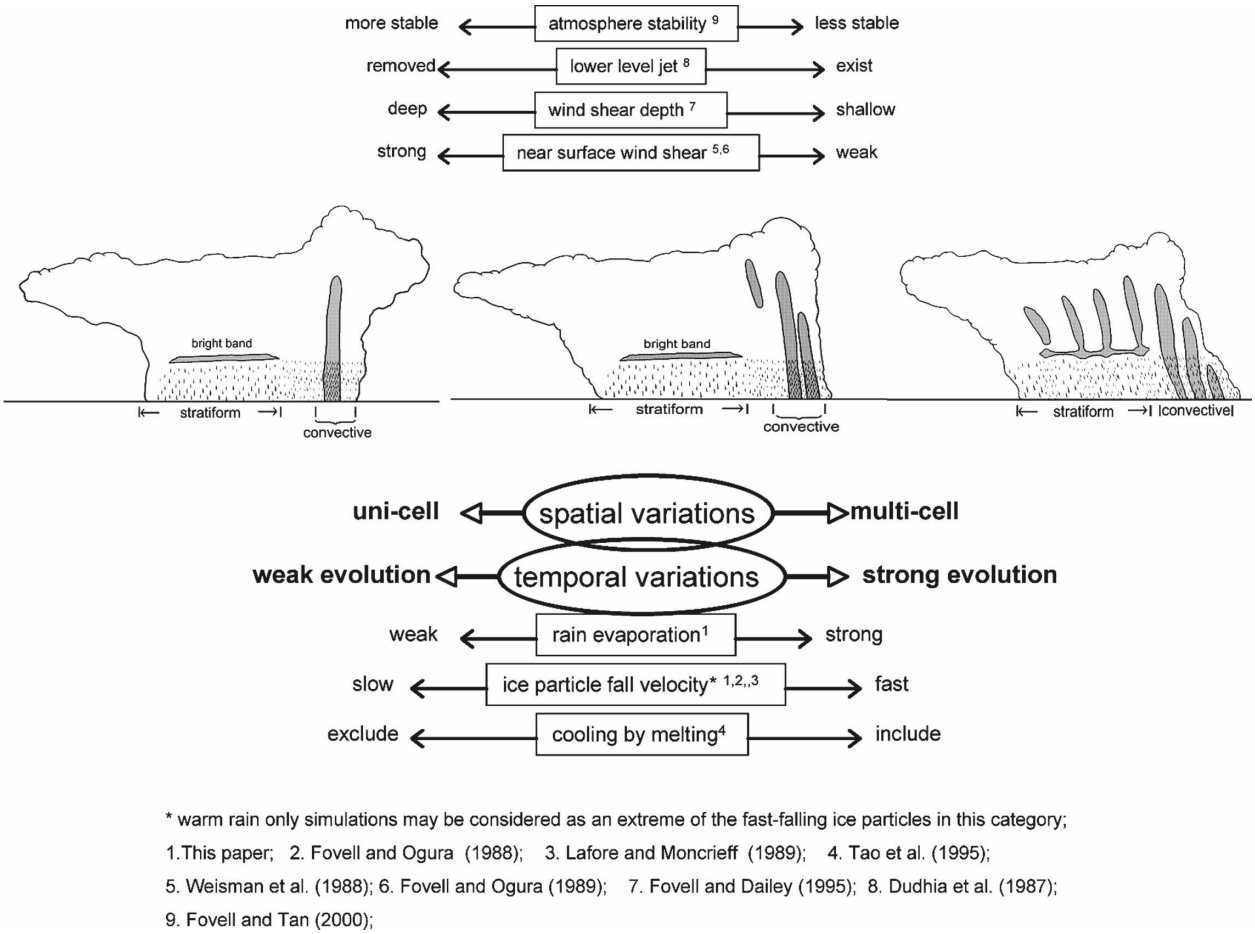

FIG. 16. Diagram summarizing factors that affect the spatial and temporal variation modes of leading convection. Environmental factors are listed in the upper half and microphysical factors in the lower half of the diagram.

ice phase particles to be transported rearward to the stratiform region—show a considerable increase in the stratiform portion of the storm. First, the rainfall rate in the deep downdraft immediately behind the leading convection is reduced, resulting in less rain evaporation and a weaker cool pool. Second, the extensive stratiform region enhances the midlevel RTF flow and the shear associated with it, which counteracts the vorticity generated by the cool pool itself. Overall, more extensive trailing stratiform rain weakens the cool pool circulation and promotes a more upright leading cell. Sensitivity tests that either increase the amount of the slow-falling species (snow) at the expense of the fast-falling species (hail/graupel) or reduce the density and fall velocity of the fast-falling species generally produce a wider stratiform region, more upright leading convection, and a weaker leading cell regeneration cycle.

An empirical correction factor—$r(q_r) = 0.11q_r^{-1.27} + 0.98$, where q_r is the rain mixing ratio (g kg^{-1})—is developed to correct the overestimation of rain evaporation in the bulk scheme. Applying $r(q_r)$ in the bulk scheme produces spatial and temporal variation modes similar to those in sensitivity tests using the mean evaporation reduction factor. However, using $r(q_r)$ consistently results in a larger stratiform area. Similarly, it is possible to tune ice phase microphysics in the bulk simulation using the bin scheme. However, ice phase microphysics has many uncertainties, including ice initiation and multiplication and the density, shape, and terminal fall velocity of various ice species and their interactions with one another. Many fundamental processes in ice microphysics are still being actively researched. Planned future study includes validating the ice microphysics in the bin scheme using both in situ and remote observations. After gaining confidence in the bin simulation, it will then be used to improve bulk microphysical schemes.

A spectrum of MCSs with various sizes of trailing stratiform regions and spatial and temporal variation

modes in between the original bulk and bin microphysical simulations have been achieved by tuning the bulk scheme parameters in this study. A review of previous modeling studies shows that the same spectrum of storm structures may be simulated by varying environmental conditions over wide ranges, as summarized in Fig. 16. The unicell and multicell storm are at two ends of the spatial variation spectrum, and weak and strong evolution are at two ends of the temporal variation mode. Although a unicell storm is always associated with the weak evolution mode in our simulations, the spatial and temporal variations along the spectrum do not always synchronize. For example, there are multicell storms with rather weak cell regeneration.

In Fig. 16, microphysical factors affecting the simulated MCS structures are summarized below the schematic illustrations, and the environmental factors above them. Different representations of rain evaporation rates and ice particle fall velocities, as well as of the melting process, can produce similar sensitivities, as does varying the strength and depth of the environmental wind shear, lower-level jet, and atmospheric stability. Summaries in Fig. 16 show the importance of accurately representing key microphysical processes to produce a realistic MCS. Many previous MCS simulations show predominantly multicell structures. Even when a unicell storm was simulated, it was sometimes considered unrealistic (e.g., Dudhia et al. 1987) because of its narrow stratiform region. In this study, a unicell storm with a weak evolution mode that compares well with observations is achieved through the bin microphysical scheme simulation. It is shown that a MCS may be able to maintain a unicell, weak evolution mode for hours. This provides further modeling support for the storm regeneration modes observed in, for example, Foote and Frank (1983). However, very high-resolution (both spatial and temporal) radar observations are needed to further determine the frequencies and detailed structures of MCS systems with different spatial and temporal variations modes and to validate the model simulations.

Acknowledgments. The authors wish to thank Steve Palm and Glen Engel-Cox for editing and Jenny Zeng for her help in drawing figures. Constructive suggestions from Professor Robert Fovell and anonymous reviewers have greatly improved this paper. This research is mainly supported by the NASA headquarters and the NASA TRMM and PMM missions. The authors are grateful to Dr. R. Kakar at NASA headquarters for his support of this research. Acknowledgement is also made to NASA GSFC for computer time used in this research.

REFERENCES

Dudhia, J., M. W. Moncrieff, and D. W. K. So, 1987: The two-dimensional dynamics of West African squall lines. *Quart. J. Roy. Meteor. Soc.,* **113,** 121–146.

Ferrier, B. S., J. Simpson, and W.-K. Tao, 1996: Factors responsible for precipitation efficiencies in midlatitude and tropical squall simulations. *Mon. Wea. Rev.,* **124,** 2100–2125.

Foote, G. B., and H. W. Frank, 1983: Case study of a hailstorm in Colorado. Part III: Airflow from triple-Doppler measurements. *J. Atmos. Sci.,* **40,** 686–707.

Fovell, R. G., and Y. Ogura, 1988: Numerical simulation of a midlatitude squall line in two dimensions. *J. Atmos. Sci.,* **45,** 3846–3879.

——, and ——, 1989: Effect of vertical wind shear on numerically simulated multicell storm structure. *J. Atmos. Sci.,* **46,** 3144–3175.

——, and P. S. Dailey, 1995: The temporal behavior of numerically simulated multicell-type storms. Part I: Modes of behavior. *J. Atmos. Sci.,* **52,** 2073–2095.

——, and P.-H. Tan, 2000: A simplified squall-line model revisited. *Quart. J. Roy. Meteor. Soc.,* **126,** 173–188.

Fritsch, J. M., R. J. Kane, and C. R. Chelius, 1986: The contribution of mesoscale convective weather systems to the warm-season precipitation in the United States. *J. Climate Appl. Meteor.,* **25,** 1333–1345.

Houze, R. A., Jr., 2004: Mesoscale convective systems. *Rev. Geophys.,* **42,** RG4003, doi:10.1029/2004RG000150.

Hu, Z., and R. C. Srivastava, 1995: Evolution of raindrop size distribution by coalescence, breakup, and evaporation: Theory and observations. *J. Atmos. Sci.,* **52,** 1761–1783.

Johnson, R. H., and P. J. Hamilton, 1988: The relationship of surface pressure features to the precipitation and airflow structure of an intense midlatitude squall line. *Mon. Wea. Rev.,* **116,** 1444–1472.

Kessler, E., III, 1969: *On the Distribution and Continuity of Water Substance in Atmospheric Circulation. Meteor. Monogr.,* No. 32, Amer. Meteor. Soc., 84 pp.

Lafore, J.-P., and M. W. Moncreiff, 1989: A numerical investigation of the organization and interaction of the convective and stratiform regions of tropical squall lines. *J. Atmos. Sci.,* **46,** 521–544.

Lang, S., W.-K. Tao, R. Cifelli, W. Olson, J. Halverson, S. Rutledge, and J. Simpson, 2007: Improving simulations of convective systems from TRMM LBA: Easterly and westerly regimes. *J. Atmos. Sci.,* **64,** 1141–1164.

Li, X., W.-K. Tao, A. P. Khain, J. Simpson, and D. E. Johnson, 2009: Sensitivity of a cloud-resolving model to bulk and explicit bin microphysical schemes. Part I: Comparisons. *J. Atmos. Sci.,* **66,** 3–21.

Lin, Y.-L., R. D. Farley, and H. D. Orville, 1983: Bulk parameterization of the snow field in a cloud model. *J. Climate Appl. Meteor.,* **22,** 1065–1092.

McCumber, M., W.-K. Tao, J. Simpson, R. Peng, and S.-T. Soong, 1991: Comparison of ice-phase microphysical parameterization schemes using numerical simulations of tropical convection. *J. Climate Appl. Meteor.,* **30,** 985–1004.

Pruppacher, H. R., and J. D. Klett, 1997: *Microphysics of Clouds and Precipitation.* 2nd ed. Kluwer Academic, 954 pp.

Rosenfeld, D., and C. W. Ulbrich, 2003: Cloud microphysical properties, processes, and rainfall estimation opportunities. *Radar and Atmospheric Science: A Collection of Essays in*

Honor of David Atlas, Meteor. Monogr., No. 52, Amer. Meteor. Soc., 237–258.

Rotunno, R., J. B. Klemp, and M. L. Weisman, 1988: A theory for strong, long-lived squall lines. *J. Atmos. Sci.,* **45,** 463–485.

Rutledge, S. A., and P. V. Hobbs, 1984: The mesoscale and microscale structure and organization of clouds and precipitation in midlatitude cyclones. XII: A diagnostic modeling study of precipitation development in narrow cold-frontal rainbands. *J. Atmos. Sci.,* **41,** 2949–2972.

Tao, W.-K., J. R. Scala, B. Ferrier, and J. Simpson, 1995: The effect of melting processes on the development of a tropical and a midlatitude squall line. *J. Atmos. Sci.,* **52,** 1934–1947.

Thompson, G., R. M. Rasmussen, and K. Manning, 2004: Explicit forecasts of winter precipitation using an improved bulk microphysics scheme. Part I: Description and sensitivity analysis. *Mon. Wea. Rev.,* **132,** 519–542.

Tzivion, S., G. Feingold, and Z. Levin, 1989: The evolution of raindrop spectra. Part II: Collisional collection/breakup and evaporation in rainshaft. *J. Atmos. Sci.,* **46,** 3312–3327.

Weisman, M. L., 1992: The role of convectively generated rear-inflow jets in the evolution of long-lived mesoconvective systems. *J. Atmos. Sci.,* **49,** 1826–1847.

——, and R. Rotunno, 2004: "A theory for strong long-lived squall lines" revisited. *J. Atmos. Sci.,* **61,** 361–382.

——, J. B. Klemp, and R. Rotunno, 1988: Structure and evolution of numerically simulated squall lines. *J. Atmos. Sci.,* **45,** 1990–2013.